

Assessing Optical and Electrical Properties of Highly Active IrO_x Catalysts for the Electrochemical Oxygen Evolution Reaction via Spectroscopic Ellipsometry

René Sachse, Mika Pflüger, Juan-Jesús Velasco-Vélez, Mario Sahre, Jörg Radnik, Michael Bernicke, Denis Bernsmeier, Vasile-Dan Hodoroaba, Michael Krumrey, Peter Strasser, Ralph Kraehnert,* and Andreas Hertwig*

Cite This: *ACS Catal.* 2020, 10, 14210–14223

Read Online

ACCESS |

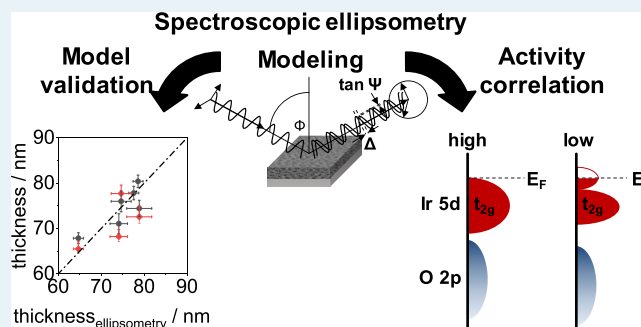
Metrics & More

Article Recommendations

Supporting Information

ABSTRACT: Efficient water electrolysis requires highly active electrodes. The activity of corresponding catalytic coatings strongly depends on material properties such as film thickness, crystallinity, electrical conductivity, and chemical surface speciation. Measuring these properties with high accuracy in vacuum-free and non-destructive methods facilitates the elucidation of structure–activity relationships in realistic environments. Here, we report a novel approach to analyze the optical and electrical properties of highly active oxygen evolution reaction (OER) catalysts via spectroscopic ellipsometry (SE). Using a series of differently calcined, mesoporous, templated iridium oxide films as an example, we assess the film thickness, porosity, electrical resistivity, electron concentration, electron mobility, and interband and intraband transition energies by modeling of the optical spectra. Independently performed analyses using scanning electron microscopy, energy-dispersive X-ray spectroscopy, ellipsometric porosimetry, X-ray reflectometry, and absorption spectroscopy indicate a high accuracy of the deduced material properties. A comparison of the derived analytical data from SE, resonant photoemission spectroscopy, X-ray absorption spectroscopy, and X-ray photoelectron spectroscopy with activity measurements of the OER suggests that the intrinsic activity of iridium oxides scales with a shift of the Ir 5d t_{2g} sub-level and an increase of p–d interband transition energies caused by a transition of μ_1 -OH to μ_3 -O species.

KEYWORDS: spectroscopic ellipsometry, electrocatalysis, oxygen evolution reaction, mesoporous iridium oxide films, non-destructive ambient analysis, intrinsic OER activity, complementary methodology and metrology



INTRODUCTION

Porous materials, like metal oxides, are versatile and attractive candidates for energy-related applications, for instance, photo-voltaics,^{1–3} electrolysis,^{4–6} or batteries^{7–10} due to their high surface to volume ratio and improved accessibility of active sites. The activity of porous materials in electrochemical reactions is highly dependent on their properties, i.e., film thickness, crystallinity, electrical conductivity, porosity, and chemical composition. Oxides based on iridium, ruthenium, and titanium catalyze the oxygen evolution reaction (OER) under acidic conditions.^{11–13} Moreover, mixed oxides of similar compositions (e.g., IrO_x-TiO_x) are applied in the industrial production of chlorine via electrolysis of NaCl as well as HCl.^{14,15} Catalytically active oxide coatings can be synthesized via different methods, including sputtering,^{16–18} electrodeposition,^{19,20} spray deposition,²¹ or chemical methods.^{22–24} The resulting activity, selectivity, and stability are strongly influenced by the respective oxide composition, which

in turn are defined by the chosen synthesis approach and synthesis conditions.^{25,26}

Key to the development of improved catalysts is an improved understanding of the relations between their performance, stability, and physicochemical properties. Due to the nature of surface catalysis, a material's electronic properties are of particular interest because they can reveal atomistic information related to the active sites. Advanced optical spectroscopy can reveal some of these properties. Goel et al. measured the energy-dependent reflectivity of IrO₂ and RuO₂ single crystals.²⁷ They compared the imaginary part of the dielectric function (ϵ_2) with the band structure and density

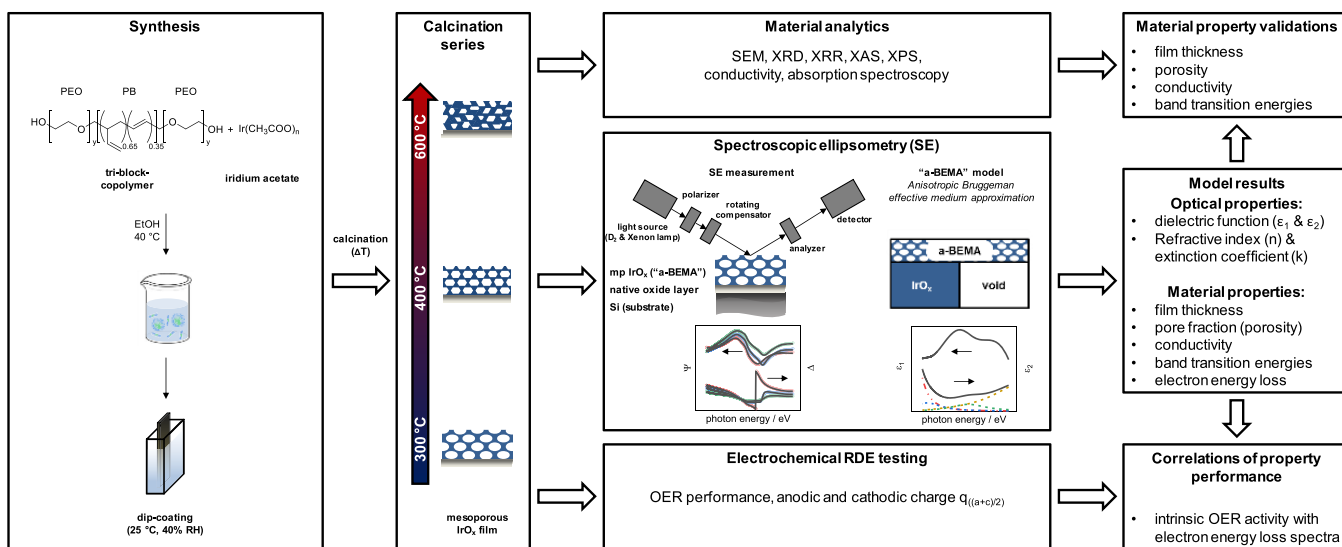
Received: August 31, 2020

Revised: October 29, 2020

Published: November 20, 2020



Scheme 1. Illustration of the Evaluation Procedure of Mesoporous Iridium Oxide Films with Spectroscopic Ellipsometry, Including the Synthesis and Calcination at Temperatures between 300 and 600 °C as Well as Film Analysis and Correlation of Material Properties with Electrochemical Performance



of states (DOS) and concluded that features below 2.5 eV can be assigned to free-carrier absorption and d–d intraband transition. Above 3 eV, all features in the ϵ_2 were attributed to p–d interband transitions. Kawar et al. studied spray-deposited iridium oxides by a combination of Raman and IR spectroscopy and resistivity measurements.²⁸ Optical transitions were assigned to d–d intraband transition. With increasing annealing temperature, a change from semiconductor to metallic behavior was observed. Also, impurities, crystalline defects, and grain boundaries affect the electrical conductivity of iridium oxide and might be accessible via optical spectroscopy.^{28,29} However, quantitative correlations between OER performance and the catalyst's optical properties have been rarely established. This results from the significant challenges faced in attempts to prepare highly active catalysts in an environment that enables advanced optical spectroscopy with sufficiently accurate results.

We recently established nanostructured oxide films as model materials for, e.g., the analysis of temperature-induced phase transitions in iron oxide via low-energy electron microscopy (LEEM),³⁰ the analysis of superparamagnetic effects,³¹ and an improved understanding of electrical conductivity in IrO_x - TiO_x mixed oxides^{32,33} as well as the elucidation of activity-controlling parameters in iridium oxide.¹² The oxide films are synthesized in the form of homogeneous, nanostructured films with an optical quality on substrates (e.g., silicon, silica, or titanium) suited for the respective experiments. The synthesis relies on dip-coating a solution containing suitable precursors, polymeric templates and solvents, evaporation-induced self-assembly (EISA) during deposition, and subsequent thermal treatments. The treatment results in template removal, formation of a defined mesoporous structure and crystallization of the oxide framework.^{34,35} Via appropriate choice of the synthesis parameters, many of the oxides properties, e.g., the composition, crystallinity, and porosity, can be controlled and systematically varied in a wide range. Hence, the related changes in catalytic performance can be studied.

Ellipsometry is a very versatile spectroscopic method, often used to study film thicknesses and refractive indexes, which is

also in context with oxide films with templated nanostructure.^{36–38} In environmental ellipsometric porosimetry (EEP), i.e., the measurement of the refractive index in combination with humidity-controlled condensation of different solvents inside the pores, the porosity and pore-size distribution can be derived.^{34,39} Furthermore, optical and electronic properties such as dielectric functions (real ϵ_1 and imaginary part ϵ_2) or optical constants (refractive index n and extinction coefficient k), the electrical resistivity (ρ), optical band gaps (E_g), and band-to-band transitions can be determined by spectroscopic ellipsometry (SE).^{40–44} Moreover, these properties can be assessed in a non-destructive way under vacuum-free and even environmental conditions.^{40,45} Previous studies on mesoporous, templated titanium oxides show that the layer thickness and porosity can be evaluated via SE,⁴⁶ cross-sectional SEM, and electron probe microanalysis (EPMA) by using EDS⁴⁷ or EEP.⁴⁸

Unfortunately, the material properties cannot be derived directly from the measured spectra. A model analysis has to be performed to fit the measured spectra of the amplitude ratio ($\tan(\Psi)$) and phase difference (Δ). From the model parameters, the material properties can be deduced. In consequence, suitable models have to be developed and validated before they can be applied under environmental or operando conditions.

We propose a model for the ellipsometric fit studies of metal oxides in electrocatalysis. Moreover, we develop and validate the respective SE models via SEM, X-ray reflectometry (XRR), a combined analysis approach of EPMA-EDS with the thin-film software package StrataGem, and ellipsometric porosimetry (EP). We also compared the electronic structure of the catalysts from calculated valence electron energy loss spectra (VEELS) by resonant photoemission spectroscopy (ResPES), X-ray absorption spectroscopy (XAS), and X-ray photoelectron spectroscopy (XPS). Mesoporous iridium oxide films serve as an example for a highly active OER catalyst.

The methodology is outlined in Scheme 1. In a first step, mesoporous iridium oxide films are synthesized on different substrates via nano-casting as described in detail in refs 12 and 49. The material's crystallinity, porosity, and catalytic activity

are varied by a systematic calcination series ranging from 300 to 600 °C. All samples of the series are analyzed via SE. An SE model for the whole calcination series is developed based on an anisotropic Bruggeman effective medium approximation (a-BEMA). By modeling the measured Ψ and Δ spectra, the film thickness, porosity, electrical resistivity, and transition energies were obtained and validated by independently performed analyses via SEM, XRR, EP, resistivity measurements, and UV–vis–NIR absorption spectroscopy. To assess the catalytic properties, the OER performance, stability, and surface-charge normalized (intrinsic) activity were measured via cyclic voltammetry for the sample series. Finally, possible correlations between performance descriptors and material properties were assessed. A comparison between the valence electron energy loss spectra (VEELS) derived from the real (ϵ_1) and imaginary parts (ϵ_2) of the dielectric function from SE measurements and the catalytic results reveals a direct correlation between the intensity of p–d interband transitions and the surface-charge normalized OER activity. This result was supported by XAS at the O K edge, ResPES in the vicinity of the O 1s absorption edge, and XPS measurements.

EXPERIMENTAL SECTION

Chemicals. For the synthesis of mesoporous iridium oxide films, iridium acetate ($\text{Ir}(\text{CH}_3\text{COO})_n$, 99.95% metals basis, ca. 48% Ir) was used from chemPUR and a triblock copolymer (PEO-PB-PEO, containing 20,400 g mol⁻¹ polyethylene oxide (PEO) and 10,000 g mol⁻¹ polybutadiene (PB)) was purchased from Polymer Service Merseburg GmbH.⁵⁰ Ethanol (EtOH, >99%) was used as solvent from Sigma-Aldrich. All chemicals were used as received. Three different classes of Si wafers were used as substrates and are characterized by single side-polished Si wafers with a (100) orientation (Siegert Wafers) and Si wafers (111) with a thermal SiO₂ layer from Silicon Materials with nominal SiO₂ thicknesses of 150 nm and ca. 1000 nm, respectively. Si wafers were cleaned with ethanol prior to film deposition. For electrical conductivity measurements, IrO_x films were deposited on glass substrates, which were cleaned with ethanol prior to film deposition. Electrochemical measurements were carried out on conductive titanium substrates, which were polished with a 0.02 μm non-crystallizing amorphous colloidal silica suspension (Buehler, MasterMet 2) and subsequently cleaned in ethanol. Iridium foil (0.25 mm-thick, 99.8% (metals basis), 22.7 g cm⁻³) was purchased from abcr chemicals GmbH and used as the Ir reference material for the EPMA quantification. Further, a TiO₂ reference material was used as the O reference and a Si wafer from Siegert Wafers was used as Si reference.

Synthesis of Iridium Oxide Films. Iridium oxide films were synthesized according to the synthesis described by Ortel et al.⁴⁹ In a slightly modified synthesis, 169 mg of the PEO-PB-PEO polymer template was dissolved in 7.5 mL of ethanol at 40 °C. After complete dissolution, 844 mg of iridium(III) acetate was added and mixed for 1 h at 40 °C. The dip-coating solution was transferred into a preheated Teflon cuvette (2 h at 50 °C), and dip-coating was immediately performed under controlled conditions (25 °C, 40% relative humidity) with a withdrawal rate of 200 mm min⁻¹. The as-synthesized films were dried for 5 min under the same conditions and subsequently calcined in a preheated furnace in flowing air for 5 min at temperatures between 300 and 600 °C.

Physicochemical Characterization. SEM images were recorded on a JEOL 7401F at 10 kV and evaluated with ImageJ

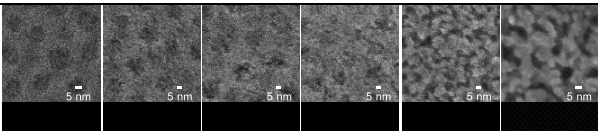
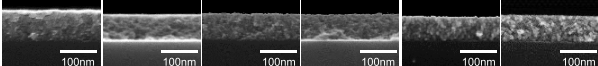
software (v. 1.51w, www.imagej.nih.gov/ij/) with respect to the film thickness and pore ordering and size. Energy-dispersive X-ray spectra for the electron probe microanalysis (EPMA) were taken with a Zeiss SEM of type Supra 40 equipped with a Schottky field emitter and an energy-dispersive X-ray spectrometer (EDS) with a 10 mm² LN₂-free silicon drift detector (SDD) and an energy resolution of 123 eV (Bruker XFlash 5010). X-ray intensities of interest were divided by the electron probe current and live time to calculate k_{EPMA} values (different from the extinction coefficient k from ellipsometry). The k_{EPMA} values are the ratio of the X-ray intensity of the element to be examined in the unknown sample to the X-ray intensity of the same element in a sample of known elemental concentration. Accelerating voltages of 15, 20, 25, and 30 kV were used to calculate the k_{EPMA} values of Ir $L\alpha$, O $K\alpha$, and Si $K\alpha$. EPMA is based on a quantification model from Pouchou using the thin-film analysis software StrataGem (v. 6.7 SAMx, Guyancourt, France).⁵¹ The software iteratively fits the calculated k_{EPMA} values to the measured ones with the mass deposition as the final result. Typically, the StrataGem software converts mass deposition into film thickness after specification of the film density. However, the reverse approach can also be used to determine film the density from mass deposition and the film thickness measurement.⁴⁷ The average film density was used to calculate the porosity of the sample by dividing the theoretical density of crystalline IrO₂ ($\rho = 11.66 \text{ g cm}^{-3}$) by the measured film density.

X-ray reflectometry (XRR) and X-ray diffraction measurements (XRD) were performed at a Bragg–Soller X-ray diffractometer system with a flat secondary monochromator and fixed Cu $K\alpha$ tube (Seifert XRD 3000TT). Furthermore, XRR was performed at the four-crystal monochromator beamline in the laboratory of Physikalisch-Technische Bundesanstalt⁵² at the BESSY II storage ring in Berlin. The beamline includes a monochromator allowing the adjustment of the photon energy in the range between 1.7 and 10 keV,⁵³ several slits, and two pinhole stages for beam shaping. The sample chamber⁵⁴ allows the positioning of the sample in all three directions with a precision of 3 μm and the rotation of the sample around all three axes with a precision of 0.001°. The whole beam path including the sample site is evacuated and a high vacuum is maintained. The intensity of the direct X-ray beam without the sample and the reflected beam from the sample is measured using a photodiode. At photon energies above ca. 3 keV, the intensity of the direct beam is monitored during measurement using a thin transmission Si photodiode. All samples were measured using the Cu $K\alpha$ lab instrument, and a 375 °C sample was selected to be additionally measured at the synchrotron beamline at a photon energy of 8048 eV. This measurement was taken to be directly comparable with the Cu $K\alpha$ measurements.

UV–vis–NIR absorption spectroscopic measurements on mesoporous iridium oxide films deposited on glass substrates were carried out with a Varian Cary 5000 in a spectral range of 350–1000 nm with 1 nm steps. An uncoated glass substrate was used as a reference sample.

Sheet conductivity measurements were carried out with both an MR-1 surface resistance device (Schuetz Messtechnik) equipped with a four-point pin probe head and a Keithley Electrometer Model 6517B relying on a two-point measurement principle having a probe head characterized by 8 × 8 pins with altering polarity.

Table 1. Summary of the Derived Film Property Values from the Different Measurement Methods Used for the Analysis and Comparison of the Mesoporous Iridium Oxide Films

Method	Property	$T_{\text{calc.}}$					
		300 °C	350 °C	375 °C	400 °C	500 °C	600 °C
material properties							
SEM	top-view						
	cross-section						
	pore size / nm	15.1	14.7	16.0	14.0		
	thickness / nm	80.4	67.9	76.0	74.4	71.1	77.8
EPMA-EDS / StrataGem	mass-deposition / $\mu\text{g cm}^{-2}$	30.48	25.50	33.82	36.89	34.99	39.70
	density / g cm^{-3}	3.79	3.76	4.45	4.96	4.92	5.10
	porosity ^a / %	67.5	67.8	61.8	57.5	57.8	56.3
XRR	thickness / nm	(80.9)	65.5	77.7	72.5	68.2	
	density / g cm^{-3}	4.60	5.41	6.77	7.61	8.50	
	porosity ^a / %	60.6	53.6	41.9	34.8	27.1	
ellipsometric porosimetry	porosity / %	52.3	45.1	44.6	41.8	39.6	
conductivity measurement	resistivity ρ_R^b / Ohm cm	$2.17 \cdot 10^{-3}$	$2.27 \cdot 10^{-3}$	$1.92 \cdot 10^{-3}$	$1.52 \cdot 10^{-3}$	$7.81 \cdot 10^{-4}$	$5.35 \cdot 10^{-4}$
	resistivity ρ_R^c / Ohm cm	$1.87 \cdot 10^{-3}$	$1.18 \cdot 10^{-3}$	$1.35 \cdot 10^{-3}$	$9.36 \cdot 10^{-4}$	$6.37 \cdot 10^{-4}$	$3.31 \cdot 10^{-4}$
UV-Vis-NIR absorption spectroscopy	Ir 5d transition energy / eV	3.14	3.12	3.13	3.18	3.26	3.29
electrochemical testing							
OER	$j_{1.55V}$ CV 2 / mA cm^{-2}	20.2	21.6	19.6	15.5	2	0.6
	$j_{1.55V}$ CV 50 / mA cm^{-2}	16.8	17.5	16.3	12.7	1.5	0.3
	$q_{(a+c)2}$ / C	$6.3 \cdot 10^{-3}$	$6.7 \cdot 10^{-3}$	$5.9 \cdot 10^{-3}$	$4.6 \cdot 10^{-3}$	$1.2 \cdot 10^{-3}$	$4.7 \cdot 10^{-4}$
	intrinsic activity CV 2 / $\text{mA cm}^{-2} \text{C}^{-1}$	3200	3208	3278	3335	1651	1348
	intrinsic activity CV 50 / $\text{mA cm}^{-2} \text{C}^{-1}$	2665	2600	2735	2729	1202	530
spectroscopic ellipsometric measurements and modeling							
spectroscopic ellipsometry	thickness / nm	78.6	64.7	74.2	78.9	74.1	77.6
	porosity / %	48.8	46.5	46.4	44.3	42.8	45.8
	resistivity ρ_R / Ohm cm	$1.13 \cdot 10^{-3}$	$1.10 \cdot 10^{-3}$	$9.74 \cdot 10^{-4}$	$9.31 \cdot 10^{-4}$	$6.38 \cdot 10^{-4}$	$4.48 \cdot 10^{-4}$
	electron concentration N / cm^{-3}	$7.14 \cdot 10^{21}$	$7.35 \cdot 10^{21}$	$7.54 \cdot 10^{21}$	$8.76 \cdot 10^{21}$	$1.24 \cdot 10^{22}$	$1.25 \cdot 10^{22}$
	electron mobility μ / $\text{cm}^2 \text{V}^{-1} \text{s}^{-1}$	0.774	0.772	0.849	0.765	0.791	1.119
	mean scattering time τ / fs	0.440	0.439	0.483	0.435	0.450	0.636
	Ir 5d transition energy / eV	3.17	3.09	3.06	3.08	3.2	3.29

^aReference density: 11.66 g cm^{-3} (crystalline IrO_2). ^bSheet conductivity measurements with a two-point pin probe head. ^cSheet conductivity measurements with a four-point pin probe head.

SE measurements were performed with a variable angle spectroscopic ellipsometer M2000 DI (J.A. Woollam) in a spectral range between 192 and 1697 nm. Mesoporous iridium oxide films deposited on single side-polished (100) silicon substrates and films deposited on single side-polished (111) silicon substrates with thermal silicon dioxide layers (ca. 150 nm and ca. 1000 nm) were measured at angles of incidence (AOIs) of 65° , 70° , and 75° relative to normal. Ψ and Δ spectra were analyzed with CompleteEASE software (v6.42). The used model consists of a silicon substrate with a native oxide layer (3 nm for substrates without a thermal SiO_2 layer) or a Si/ SiO_2 interface layer (1 nm for substrates with a thermal SiO_2 layer), a SiO_2 layer for the Si substrates with thermal SiO_2 , and an a-BEMA (see Section S5 for further details).

Ellipsometric porosimetry (EP) measurements were carried out by fitting an environmental cell on the ellipsometer with a fixed angle of incidence of 60° . The relative humidity was adjusted by mixing dry nitrogen gas with water-saturated nitrogen gas, obtained by water bubbling prior to entering the

mixing chamber. The total N_2 flux amounted to 2.5 L min^{-1} , controlled by two mass flow controllers, and a constant temperature of 23°C . The relative humidity was measured for the outgoing gas and for each water partial pressure behind the cell. The evaluation of the refractive index as a function of the relative humidity was carried out at 2.6 eV (474 nm).

ResPES, XAS, and XPS spectra were collected in the ISS beamline in BESSY II (Berlin), which is equipped with a SPECS PHOIBOS 150 NAP hemispherical analyzer. Synchrotron X-ray radiation is sourced from a bending magnet (D41) and a plane monochromator (PGM) with an excitation energy ranging from 80 to 2000 eV (soft X-ray) and with a flux of 6×10^{10} photons s^{-1} with a 0.1 A ring current with a 111 μm exit slit and $80 \mu\text{m} \times 200 \mu\text{m}$ beam spot size.

Electrochemical Testing. Electrocatalytic measurements were performed in a three-electrode disc setup (Pine MSR rotator, BioLogic SP-200 potentiostat). A reversible hydrogen electrode (RHE, Gaskatel, HydroFlex) was used as a reference, Pt gauze (Chempur, 1024 mesh cm^2 , 0.06 mm wire diameter,

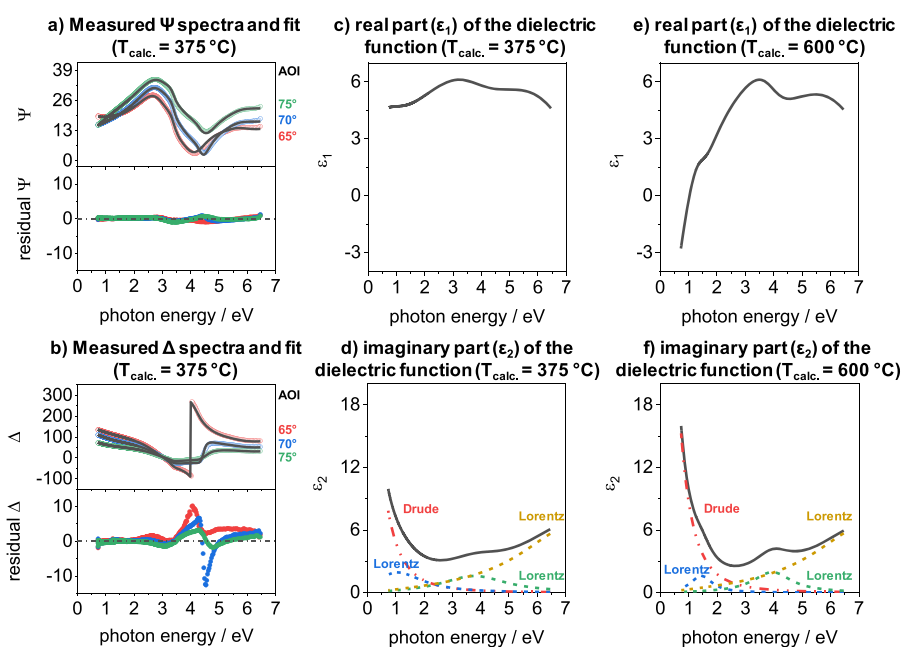
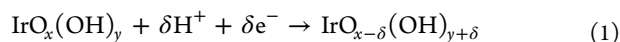


Figure 1. Measured Ψ (a) and Δ spectra (b) of a mesoporous IrO_x film calcined at $375\text{ }^\circ\text{C}$ and their fit results as well as the real (ϵ_1) and imaginary (ϵ_2) parts of the dielectric functions of the IrO_x material of films calcined at $375\text{ }^\circ\text{C}$ (c, d) and $600\text{ }^\circ\text{C}$ (e, f).

99.9% purity) as counter electrode, and coated titanium disks (5 mm in diameter) as a working electrode. All potentials are recorded under room temperature and referred to the RHE. Mesoporous, IrO_x -coated titanium disks were mounted in a rotating disk shaft and rotated at a speed of 1600 rpm during EC testing. Sulfuric acid was employed as electrolyte solution (0.5 M H_2SO_4 , Fixanal, Fluka Analytical) and was purged with nitrogen prior to catalytic testing. OER activity was investigated by 50 cyclic voltammograms in a potential window between 1.2 and 1.65 V_{RHE} at a scan rate of 6 mV s^{-1} . Prior to CV measurements, the impedance spectroscopy was measured at 1.2 V_{RHE} in order to correct recorded cyclic voltammograms for ohmic losses. Cyclic voltammetry (CV) in the range between 0.4 and 1.4 V_{RHE} with a scan rate of 50 mV s^{-1} was performed to determine the anodic and cathodic charge ($q_{(\text{a+c})/2}$). Ardizzone et al.⁵⁵ and Fierro et al.⁵⁶ described a reversible proton-inclusion mechanism, which can take place in this potential range as follows:



The more iridium is accessible and/or available, the higher the faradaic current obtained from this reaction. An expression for the accessible iridium centers is obtained by determining the mean value of the integrated anodic and cathodic scans of the resulting CV ($q_{(\text{a+c})/2}$).

RESULTS AND DISCUSSION

The following sections provide first an overview over the basic properties of the IrO_x model system as well as the catalytic behavior. Thereafter, the acquired SE data are presented. Subsequently, the material properties are deduced and validated. Finally, correlations between properties and OER performance are derived and interpreted.

Properties of the Model System. Mesoporous, templated iridium oxide films were synthesized on cleaned Si wafers, Si wafers with a thermal silicon dioxide layer, and

quartz and polished titanium substrates according to a procedure developed by Ortel et al.⁴⁹ A solution containing the dissolved template polymer PEO-PB-PEO,⁵⁰ ethanol, and iridium acetate was used for dip-coating the substrates followed by 5 min of a drying process. Subsequently, the substrates were transferred to a preheated muffle furnace and calcined in flowing air at the preset oven temperature for 5 min. Table 1 provides an overview of the employed calcination temperatures ranging from 300 to 600 $^\circ\text{C}$ as well as the analytical results and electrocatalytic data derived for each sample.

SEM images presented in Table 1 indicate the expected removal of the polymer template, locally ordered pores of approximately 14 and 16 nm in diameter on the outer surface (top view), and a uniform layer thickness (cross section, see Section S1 for further details). Increasing calcination temperatures induced crystallite growth, respective gradual sintering, and a slight decrease in film thickness. A combined analysis via SEM/EDS using the thin-film StrataGem software package (EPMA-EDS/StrataGem), as reported in ref 47, indicates an increase in the average film density from approximately 3.8 to 5.1 g cm^{-3} at higher calcination temperatures. XRR analysis also indicates an increase in film density, however, at higher overall values (see Section S2 for additional details). XRD (Section S3) indicates a low crystallinity up to 375 $^\circ\text{C}$ and reflections that become narrower at higher temperature, which can be attributed to crystalline IrO_2 rutile (PDF 00-015-0870). Measurements of the electrical conductivity reveal a highly conductive material, which becomes even more conductive at higher calcination temperature. UV-vis-NIR absorption spectroscopy indicates for samples calcined between 300 and 375 $^\circ\text{C}$ a separation of the Ir 5d t_{2g} and e_g sub-levels of approximately 3.13 eV, which shifts continuously up to 3.29 eV (600 $^\circ\text{C}$) with increasing calcination temperature.

The second section of Table 1 summarizes the results of the electrochemical tests (see Section S4 for further details) in terms of the geometric current density measured at 1.55 V_{RHE} in the 2nd ($j_{1.55V}$ CV2) and 50th cycles ($j_{1.55V}$ CV50) as well as

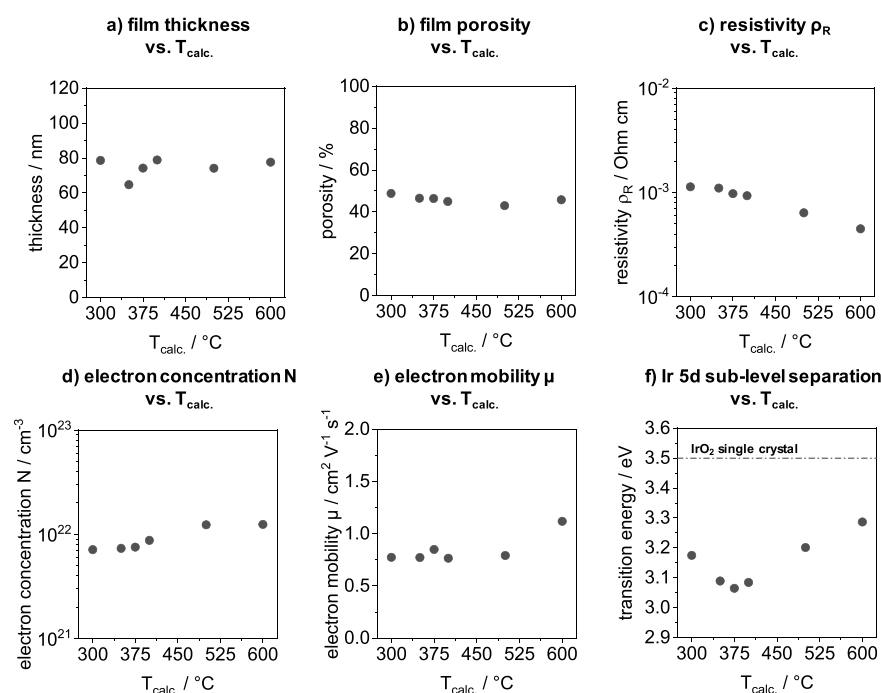


Figure 2. Layer, electrical, and optical properties of the iridium oxide material as a function of the calcination temperature. (a) Film thickness, (b) porosity, (c) resistivity, (d) electron concentration, (e) the electron mobility, and (f) Ir 5d t_{2g} and e_g sub-level separation depending on the applied calcination temperature.

the determined surface charge ($q_{(+c)}/2$) and intrinsic activity, as discussed later in the manuscript. Moreover, the material properties derived from SE analysis and the respective modeling are provided (see Section S5 for the detailed model description).

Measured and Modeled SE Spectra. SE measurements were performed on the differently calcined IrO_x films (synthesized on Si wafers as substrates) using a spectral range between 192 and 1697 nm (6.45 and 0.73 eV). The psi (Ψ) and delta (Δ) spectra were successively recorded at angles of incidence (AOIs) of 65° , 70° , and 75° at the same position on the sample. Additionally, a multi-sample approach using interference enhancement with buffer oxide layers of different thicknesses was used to improve the quality of the ellipsometric analysis. Subsequently, the measured Ψ and Δ spectra were fitted using a three-layer model comprising a silicon substrate, a native Si oxide layer (3 nm), and an a-BEMA. The a-BEMA includes the contributions of IrO_x as well as the air/void contained in the mesopores. The contribution of the oxide matrix, i.e., the real and imaginary parts of the dielectric function of the IrO_x material, was modeled by a combination of one Drude-type oscillator and three Lorentz oscillators. The model parameters of the a-BEMA (IrO_x layer thickness, air/void volume fraction, and the factor of anisotropy of pores), of the Drude-type oscillator (resistivity and mean scattering time) and the Lorentz-type oscillators (absorption strength) resulted from a standard ellipsometric fit procedure. Section S5 contains a detailed description of the ellipsometric measurement strategy and the model used.

Figure 1 presents an example of the spectra of the (a) amplitude component Ψ and (b) phase difference Δ , recorded at AOIs of 65° , 70° , and 75° for a mesoporous IrO_x film calcined in air at 375°C . Measured values (symbols) are shown along with the respective fit results (lines). Moreover, the modeling results for the same sample are displayed in terms

of (c) the real (ϵ_1) and (d) imaginary (ϵ_2) parts of the dielectric function of the IrO_x matrix. Figure 1e,f displays the corresponding data for a sample calcined at 600°C (see Section S6 for additional data).

Using the model, an excellent fit between measured and simulated Ψ and Δ spectra was achieved for all incident angles as visible in Figure 1a,b. The dielectric function obtained from the model shows for the range below 2.0 eV an increase in the imaginary (ϵ_2) part of the dielectric function toward lower photon energies, which is described by the Drude-type oscillator (Figure 1d). Additionally, a small feature indicated by a Lorentz oscillator appears near 1.0 eV. Above 2.0 eV, the absorption by two Lorentz oscillators is clearly visible. With increasing calcination temperature, a systematic change in intensity and width of the oscillators is observed (Figure 1f and Section S6), indicating a respective change of the optical and electronic properties of the IrO_x material.

Goel et al. studied an IrO_2 single crystal by reflectivity measurements in a range of 0.5 to 9.5 eV.²⁷ The iridium oxide valence band consists of oxygen p levels, while the conduction band consists of metal d levels, which further split into e_g and t_{2g} sub-levels. Goel et al. assigned the features below 2.0 eV to free-electron and intraband electronic transitions within the t_{2g} d-band complex, which can occur up to ca. 2.8 eV. Our obtained dielectric functions are in good agreement with this work. According to the Drude model, the features below 2.0 eV are interpreted as free-electron transitions. Above 3.0 eV, Goel et al. assigned three features at 3.7, 5.5, and 7.7 eV to p–d interband transition. In our spectra, we obtain two absorption features from the Lorentz oscillators around 4.0 and 7.7 eV. These features correlate to transitions from the p orbitals from the oxygen to filled and empty d-bands of the iridium.²⁷ The absence of the third feature at 5.5 eV in our spectra is likely to be related to the much lower crystallinity present in our IrO_x films compared to the single crystal of the

referenced study. Choi et al. observed in their reflectometry study on sputtered low crystalline IrO₂ films deposited on Al₂O₃ (0001) substrates only two features at approximately 4.0 to 7.0 eV.⁵⁷

The crystallinity of the studied IrO_x material strongly increases with calcination temperature (see, e.g., XRD data presented in Section S3).^{12,49} We observed corresponding changes in the dielectric function of IrO_x, e.g., an increase in free-electron absorption in the imaginary part (Figure 1d vs Figure 1f). Moreover, the features near 1.0 and 4.0 eV presented by the Lorentz oscillators become more narrow. The real part of the dielectric functions shows a strong decrease at lower photon energies for higher calcination temperatures (Figure 1c,e) and becomes zero for the film calcined at 600 °C near 1 eV. These observations agree well with the data of the single crystal where the real part of the dielectric function becomes zero at approximately 2 eV.²⁷ In general, the modeled spectra of porous iridium oxide films and the dielectric functions are consistent with reported data on crystalline IrO₂ as well as sputtered iridium oxide.^{27,57}

Material Properties Derived from SE Data. Modeling of the SE spectra recorded for differently calcined mesoporous IrO_x films provides access to numerous material properties. Figure 2 displays the (a) film thickness, (b) porosity, (c) resistivity, (d) electron concentration, (e) electron mobility, and (f) Ir 5d t_{2g} and e_g sub-level separation as a function of the applied calcination temperature. The complementary list of all parameters is reported also in Table 1.

The film thicknesses obtained from SE modeling range from 64 to 79 nm and decrease slightly with increasing calcination temperature (Figure 2a). This trend is in good agreement with previous studies on similarly prepared porous oxide films.⁴⁹ Moreover, a slight decrease in the porosity values is observed (Figure 2b), which also agrees well with our earlier findings.⁴⁹

The IrO_x materials are highly conductive (Figure 2c). The resistivity derived from the SE model decreases with increasing calcination temperature but remains approximately 10 times higher than that reported for IrO₂ ($\rho = 5 \times 10^{-5} \Omega \text{ cm}$).²⁹

The electron concentration *N* (Figure 2d) and electron mobility μ (Figure 2e) were calculated from the fit parameters of the Drude model (resistivity and mean scattering time; see Sections S5 and S7). *N* remains roughly constant up to 375 °C, i.e., in the low-crystallinity region, and increases slightly above 400 °C when the IrO_x crystallinity progressively increases (see Section S3, XRD). This observation is consistent with previous density functional theory (DFT) calculations in iridium oxide unit cells.⁵⁸ The DFT calculations indicate that decreasing lattice parameters result in a higher electron concentration.⁵⁸ In contrast, the electron mobility (Figure 2e) shows an increase only at a calcination temperature of 600 °C, i.e., when pronounced crystallite growth due to sintering has already occurred.

Figure 2f displays the energy values for the separation of the Ir 5d t_{2g} and e_g sub-levels for direct allowed transitions derived from ellipsometric modeling. Equation 2 was used for the calculation of the absorption coefficient α (cm⁻¹) from the extinction coefficient *k*

$$\alpha = \frac{4\pi k}{\lambda} \quad (2)$$

with λ as the wavelength.

Energy values can be estimated by the Tauc relation, which is typically expressed as

$$\alpha = \frac{\alpha_0 (h\nu - E_g)^n}{h\nu} \quad (3)$$

where α_0 is a constant that is proportional to the probability of an electron transition between occupied and empty states, $h\nu$ is the photon energy, and E_g is the band-gap energy or the energy of the sub-level separation.^{41,59–61} The nature of the transition can be expressed with the constant *n*, e.g., $n = 1/2$ for direct allowed transitions or $n = 2$ for indirect allowed transitions.^{41,59–61} Energy values can be obtained by extrapolation of straight line portions to the zero absorption coefficient.

The obtained values range from 3.06 to 3.29 eV, which correspond to a separation between the t_{2g} and e_g sub-levels of the Ir 5d band.²⁷ Values increase with increasing calcination temperature and could be related to the respective increase in crystallinity and a change of oxygen species. Silva et al. reported a value of 3.2 eV for the separation between the t_{2g} and e_g bands for a low-crystalline, anodically formed iridium oxide film.⁶² They attributed the low value compared to a single crystal (3.5 eV) to the amorphous nature of the film. The non-well-defined band edges present disorder-induced tails, which extend into the band gap and could be responsible for the lower values.⁶³

Validation of Properties from SE via Independent Analytical Methods. Material properties derived from SE strongly rely on the structure and quality of the optical model. Important model results were therefore measured independently via complementary analytical methods. Figure 3 displays a comparison between the SE-derived values and independently measured values for the (a) film thickness (by SEM and XRR), (b) film porosity (by EP, EPMA-EDS/StrataGem and XRR), (c) electrical resistivity (by 2-point and 4-point conductivity measurements), and (d) energy values for the

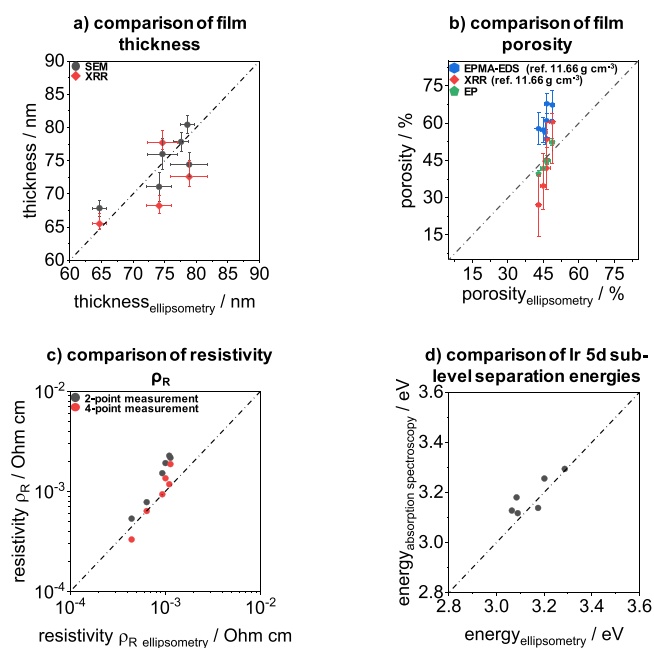


Figure 3. Comparison of layer properties by independent methods: a) film thickness by SE, XRR and SEM cross-section images, b) porosity by EPMA-EDS / StrataGem approach, SE and EP isotherms, c) resistivity by ellipsometric modeling and sheet conductivity measurements and d) energy values of Ir 5d band separation between t_{2g} and e_g sub-levels by SE and UV-vis-NIR absorption spectroscopy.

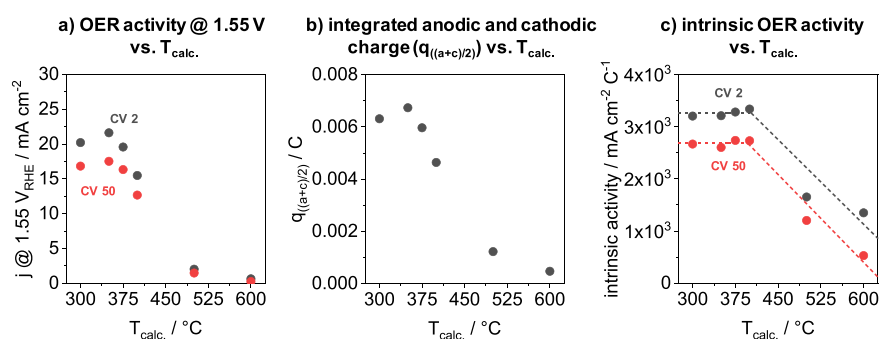


Figure 4. Electrochemical analysis of OER activity, anodic and cathodic charge, and intrinsic activity of mesoporous iridium oxide films calcined between 300 and 600 °C. (a) OER activity at a potential of 1.55 V_{RHE} of the 2nd and 50th cycle during cyclic voltammetry measurements in a potential window of 1.2–1.65 V_{RHE} and a scan rate of 6 mV s^{-1} . (b) Mean value of the integrated anodic and cathodic currents ($q_{((a+c)/2)}$) from basic cyclic voltammetry measurement in a lower potential range of 0.4–1.4 V_{RHE} and a scan rate of 50 mV s^{-1} . (c) Current density (at 1.55 V_{RHE}) normalized to the charge (intrinsic activity). All CVs were measured in N_2 purged 0.5 M H_2SO_4 and IR-corrected.

t_{2g} and e_g separation of the Ir 5d band (by UV–vis–NIR absorption spectroscopy).

The film thickness of the IrO_x calcination series as measured with SE, SEM, and XRR ranges from approximately 65 to 80 nm (Figure 3a and Table 1). The SE model, cross-sectional SEM images (Section S1), and modeling analysis of XRR measurements (Section S2) provide similar values within a 10 nm range and similar trends. The differences in the layer thickness by the three techniques are comparable with the measurement uncertainty of the individual method. Note that the different methods did not measure exactly the same location, volume, and area of the sample. We assume that uncertainty contributions from different measurement locations are possible. This was avoided as much as possible for this work; however, it is not always possible (e.g., in the case of SE vs SEM). Therefore, we carried out a homogeneity study (see Section S8 for the homogeneity study), which leads us to the assumption that inhomogeneity contributes only negligible amounts to the result uncertainties. It can be concluded that SE modeling provides an accurate determination of the layer thickness.

The porosity (Figure 3b) of the IrO_x samples in the calcination series was assessed by four different methods: SE, ellipsometric porosity sorption isotherms (see Section S9 for additional data), XRR, and a combination of SEM, EDS, and an evaluation using the software StrataGem⁵¹ (EPMA-EDS/StrataGem) as reported in ref 47. Porosities by the EPMA-EDS/StrataGem approach and XRR (measurements and fits) were calculated from the density values using the following equation:

$$P = 1 - \left(\frac{\rho_{D,\text{average}}}{\rho_{D,\text{reference}}} \right) \quad (4)$$

where P is the porosity, $\rho_{D,\text{average}}$ and $\rho_{D,\text{reference}}$ are the average and reference mass densities, respectively.

Porosity values derived from SE as well as EP range from 40 to 52%. SE and EP, the most accurate method for thin-film porosity analysis,^{33,38} agree by less than 10%. The combined method of EPMA-EDS/StrataGem yields values of approximately 56 to 68%, i.e., approximately 1.5 times higher than values derived from SE, but the trend is still captured. It is likely that the deviation results from the fact that EPMA-EDS/StrataGem method requires a bulk density of the oxide, which was assumed here to be the density of crystalline IrO_2

(11.66 g cm^{-3}). This assumption might have associated large uncertainties since the tested IrO_x samples change their crystallinity with the calcination temperature. Hackwood et al. estimated a lower density of approximately $\sim 10.0 \text{ g cm}^{-3}$ for sputtered iridium oxide.²⁹ Further, the EPMA quantification of oxygen must be considered as critical, i.e., to be associated with large uncertainties. Moreover, quantification with X-ray lines of the L series is generally less reliable than with $K\alpha$. XRR-derived porosities show a reasonable trend but larger deviations from SE data. As in the EPMA-EDS/StrataGem method, the assumption of crystalline IrO_2 with 11.66 g cm^{-3} as bulk density was used for the calculation of the porosity values, which could lead to larger uncertainties.

The electrical resistivity derived from SE agrees very well with the two-point as well as with the four-point sheet conductivity measurement (Figure 3c). Therefore, SE modeling provides a good resistivity estimate for electrically conductive IrO_x films.

Finally, Figure 3d compares the energy values of the Ir 5d band separation between the t_{2g} and e_g sub-levels obtained from SE modeling with values from UV–vis–NIR absorption spectroscopy. Again, both methods provide very similar values for the energy values of direct allowed transitions ($n = 1/2$) in the studied range.

In summary, accurate values of film thickness, porosity, resistivity, and transition energies can be determined for the studied type of IrO_x system from SE analysis, i.e., non-destructive analysis that also works under vacuum-free and even environmental conditions.

Correlating OER Activity with Material Properties.

Ultimately, the present study aims at elucidating material properties that govern and explain the catalyst's behavior in electrocatalysis as presented here. We previously reported that the OER performance of mesoporous IrO_x films is controlled by the accessible surface area and the intrinsic activity per accessible site.¹² However, the origin of an observed decrease in intrinsic activity at higher calcination temperature, i.e., higher crystallinity, could not be determined.

We therefore studied the electrocatalysis of all IrO_x samples of the calcination series (Table 1) under OER conditions. The catalysts were tested in 0.5 M H_2SO_4 via cyclic voltammetry (1.2 to 1.65 V_{RHE} , 50 cycles, 6 mV s^{-1}) in a rotating disc setup (RDE) equipped with a reversible hydrogen electrode (RHE), a Pt counter electrode, and IrO_x -coated titanium disks as a working electrode to assess the catalytic activity. From CVs

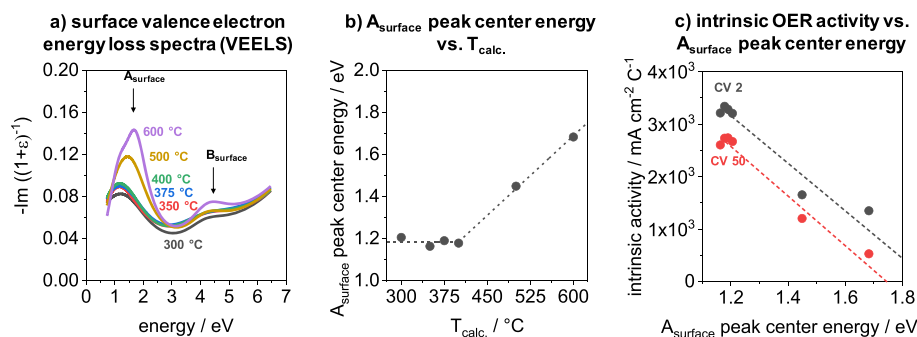


Figure 5. Valence electron energy loss spectra (VEELS) analysis and correlation between intrinsic OER activity and the shift of the peak position of mesoporous iridium oxide films calcined between 300 and 600 °C. (a) Calculated surface VEELS from the obtained real and imaginary part of the dielectric functions. (b) Peak maximum center energy of the indicated A_{surface} peak from the surface VEELS as a function of calcination temperature ($T_{\text{calc.}}$). (c) Correlation between the intrinsic OER activity and shift of the A_{surface} peak.

measured between 0.4 and 1.4 V_{RHE} (50 mV s^{-1}), the anodic and cathodic charge ($q_{(\text{a+c})/2}$) was determined as an estimate of the electrochemically accessible surface area¹² (see Section S4 for complete OER details).

Figure 4 summarizes the electrocatalytic data. The geometric current densities measured at 1.55 V_{RHE} in the 2nd ($j_{1.55\text{V}}$ CV 2) and 50th cycles ($j_{1.55\text{V}}$ CV 50) indicate the expected high OER activity for samples calcined between 300 and 375 °C with a maximum for 350 °C and a steady significant decline with increasing calcination temperature. Current densities of up to 22 mA cm^{-2} (2nd CV) and 18 mA cm^{-2} (50th CV) are observed (Figure 4a). The surface charge recorded between 0.4 and 1.4 V_{RHE} as a measure of the accessible surface area ($q_{(\text{a+c})/2}$) shows a very similar behavior (Figure 4b). In order to derive the intrinsic OER activity, the geometric current density measured at 1.55 V_{RHE} ($j_{1.55\text{V}}$) was divided by the measured surface charge ($q_{((\text{a+c})/2)}$). Consistent with our earlier analysis,¹² the intrinsic OER activity remains constant up to 400 °C but declines with further increasing the calcination temperature (Figure 4c).

Surface catalysis is governed by the electronic structure of a material. One way to assess the electronic structure is the measurement of electron energy loss spectra (EELS), which is often performed with high-energy electrons in a TEM setup. The low-loss energy region (<50 eV), so-called valence EELS, can provide information about interband transitions, dielectric properties, and plasmon excitations. Such EEL spectra in the low-loss energy region become accessible through the dielectric function derived via SE modeling.

In the dielectric formulation, the energy loss function (ELF) can be related to the single scattering distribution $S(E)$ as follows

$$S(E) = \frac{I_0 t}{\pi a_0 m_0 v^2} \text{Im}(-\epsilon(q, E)^{-1}) \ln \left[1 + \left(\frac{\beta}{\theta_E} \right)^2 \right] \quad (5)$$

where I_0 is the zero-loss intensity, t is the specimen thickness, a_0 is the Bohr radius, m_0 is the electron rest mass, v is the electron beam velocity, β is the collection semi-angle, θ_E is the characteristic scattering angle, and $\epsilon(q, E)$ is the complex dielectric function at energy-loss E and momentum transfer q .^{64–67} According to eq 5, the EEL spectra contain the complete characteristic of the complex dielectric function ϵ and the real (ϵ_1) and imaginary (ϵ_2) parts of the dielectric function can be determined by Kramers–Kronig trans-

formation for bulk and surface energy loss functions as follows:⁶⁸

bulk energy loss function(ELF)

$$\begin{aligned} &= -\text{Im}(\epsilon^{-1}) \\ &= \frac{\epsilon_2(E)}{\epsilon_1(E)^2 + \epsilon_2(E)^2} \end{aligned} \quad (6)$$

surface energy loss function(ELF)

$$\begin{aligned} &= -\text{Im}((1 + \epsilon)^{-1}) \\ &= \frac{\epsilon_2(E)}{(1 + \epsilon_1(E))^2 + \epsilon_2(E)^2} \end{aligned} \quad (7)$$

We calculated bulk and surface EEL spectra in the low-loss region from the real and imaginary parts of the dielectric functions derived from SE modeling (Section S6) for all samples of the calcination series. The calculated surface valence EEL spectra are displayed in Figure 5a. Figure 5b presents the A_{surface} peak center energy derived from the spectra as a function of the calcination temperature. Figure 5c finally reports the intrinsic OER activity (from Figure 4c) as a function of the shift in the A_{surface} peak center energy to assess correlations between the electronic structure of IrO_x and its electrocatalytic behavior (see Section S10 for complementary information on the bulk valence EEL spectra).

All samples show two peaks in the surface electron loss spectra, designated as A_{surface} and B_{surface} (Figure 5a). The A_{surface} peak maximum is located at approximately 1.2 eV for samples calcined between 300 and 400 °C. It shifts to higher energies (up to 1.7 eV) for samples calcined at 500 and 600 °C (Figure 5b). Moreover, the peak intensity increases with increasing temperature above 400 °C. The B_{surface} peak features the same center energy (4.2 eV) for all samples and increases only slightly in intensity. A similar behavior is observed for the calculated bulk valence EEL spectra (Section S10) yet with A_{bulk} at approximately 0.1 eV higher energies.

A direct comparison between the intrinsic OER activity of the studied IrO_x calcination series and the position of the A_{surface} peak energy position, as displayed in Figure 5c, indicates a direct and roughly linear correlation, both for the 2nd and 50th OER cycles. The observed shift of the peak position to a higher energy value leads to a decrease in the OER current per accessible Ir.

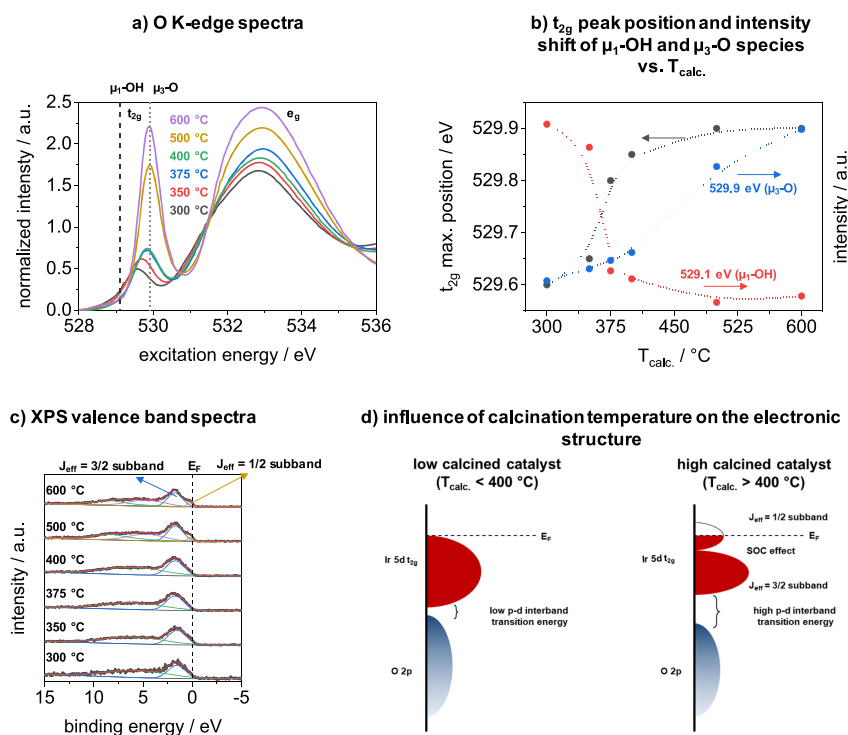


Figure 6. Analysis of the IrO_x calcination series with XAS at the O K edge and XPS measurements in the valence band as well as an illustration of the influence of the calcination temperature on the electronic structure. (a) O K edge spectra of IrO_x samples calcined between 300 and 600 °C. (b) Corresponding changes of characteristic peaks from the O K edge spectra. (c) XPS spectra in the valence band region. (d) Illustration of the dependence of the electronic structure on the calcination temperature.

According to the literature, the A_{surface} peak located at approximately 1.2 to 1.7 eV can be related to an interband transition, whereas surface and volume plasmon excitations of metal oxides occur in a different energy range of approximately 10–20 eV.^{69–73} We interpreted the observed peak as the p–d interband transition between the filled t_{2g} complex of the d-band of iridium and the p-band of the oxygen. The density of states (DOS) spectra of a single crystal indicate an interband transition between the oxygen p-bands and the iridium d-bands of approximately 1.5 to 2 eV,^{27,74} which is consistent with our observed A_{surface} peak center energy values. A change in this interband transition toward higher energies would then correlate with a lower intrinsic OER activity (Figure 5c).

To address the change in the A_{surface} peak position and correlate the VEEL spectra, we studied the electronic structure of the samples from the calcination series with XAS at the O K edge, ResPES, and XPS in the valence band. Figure 6 displays the O K edge spectra in the total electron yield (TEY) mode and the change of characteristic peaks as well as XPS measurements in the valence band and an illustration of the change of the electronic structure depending on the calcination temperature (see Section S11 for further information of ResPES and XPS).

The O K edge spectra of the samples indicate a shift of the Ir 5d t_{2g} sub-level to higher excitation energies (Figure 6a,b). Furthermore, all samples show the presence of $\mu_1\text{-OH}$ (529 eV) and $\mu_3\text{-O}$ (530 eV) species.⁷⁵ Low calcined IrO_x samples reveal more protonated $\mu_1\text{-OH}$ and less triple-coordinated oxygen $\mu_3\text{-O}$ species, while samples calcined at higher temperatures (>400 °C) show the formation of more $\mu_3\text{-O}$ species due to the formation of a rutile-like crystal structure (Figure 6b; see Section S3, XRD). The transition from protonated $\mu_1\text{-OH}$ to triple-coordinated oxygen $\mu_3\text{-O}$

species follows a similar trend as the intrinsic OER activity and the shift in the A peak from surface and bulk VEEL spectra. The same results can also be derived from the ResPES in the valence band through O 1s (see Section S10). Note that the $\mu_1\text{-OH}$ species is converted to unprotonated active $\mu_1\text{-O}$ species during OER conditions, which are the active species during the reaction conditions.⁷⁵

XPS spectra in the valence band (Figure 6c) show a small and broad peak at binding energies of approximately 5.7 eV and a characteristic peak at 1.8 eV for samples calcined between 300 and 400 °C, which can be attributed to metal–oxygen π bands and the t_{2g} sub-level of the Ir 5d orbital, respectively.^{76,77} At higher temperatures (500 and 600 °C), an additional peak at 8.1 eV and a shoulder at 0.3 eV can be observed. The peak at 8.1 eV corresponds to metal–oxygen σ bands, while the shoulder near the Fermi level can be attributed to a spin–orbital couple (SOC) splitting effect. The SOC effect splits the five electrons in the t_{2g} band into four electrons occupied as the $J_{\text{eff}} = 3/2$ sub-band and to one electron occupied as the $J_{\text{eff}} = 1/2$ sub-band.^{78–80} A similar behavior can be observed in the VEEL spectra where the higher calcined samples also show a shoulder at the A_{surface} peak (Figure 5a).

From the results of this work, we suggest that the transition from protonated $\mu_1\text{-OH}$ to triple-coordinated $\mu_3\text{-O}$ species influences the t_{2g} sub-level and therefore the p–d interband transitions between the filled t_{2g} complex of the d-band of iridium and the p-band of the oxygen. Figure 6d illustrates the dependence of the calcination temperature and thus the dependence of the oxygen species on the Ir 5d t_{2g} sub-level and the p–d interband transitions. At lower calcination temperatures, more protonated $\mu_1\text{-OH}$ species are observed, resulting in a broad t_{2g} band near the Fermi level and a low transition

energy between the O p bands and Ir d bands. With increasing calcination temperature, the transition from protonated μ_1 -OH to unprotonated μ_3 -O species occurs, shifting the t_{2g} band to higher energies thus enhancing the p–d transition energy. At high temperatures, more unprotonated μ_3 -O species are observed, leading the t_{2g} band to an SOC splitting and high p–d transition energies. Furthermore, the electrophilic character of the μ_1 -oxo species tends to a higher degree of covalence, resulting in contracted Ir–O bonds and shorter distances.^{81,82} Two possible mechanisms are proposed for the OER: (i) an acid–base mechanism in which the electrophilic oxygen of the metal-oxo species are attacked nucleophilic by the oxygen atom of the water or hydroxide and (ii) a radical coupling mechanism in which two adjacent metal-oxo species with radical characters develop molecular oxygen.^{83,84} The electrophilic character can therefore influence the catalytic rate of O–O bond formation during the OER and thus reduce the kinetic barrier of the nucleophilic attack.⁸¹ The shift of the t_{2g} band, the SOC effect, and the increase of the p–d interband transition can be observed in the O K edge, XPS valence band, and VEEL spectra calculated from SE measurements, thus explaining the origin of the intrinsic OER activity.

SUMMARY AND OUTLOOK

We present the analysis and model evaluation of mesoporous iridium oxide films with SE. The dielectric functions show the change of the amorphous character to more crystalline IrO_x films, which is consistent with measurements of the reflectance of an IrO₂ single crystal from literature. The model provides optical and electrical properties such as resistivity, electron concentration, and mobility as well as band transition energies of porous films calcined at temperatures between 300 and 600 °C. Correlations of layer properties such as the film thickness, porosity, resistivity, and intraband transition energies determined by different independent analytical methods show good agreement. Furthermore, the decrease in intrinsic OER activity at calcination temperatures above 400 °C can be explained from calculated VEEL spectra by a shift of the Ir 5d t_{2g} sub-level and the shift of p–d interband transitions to higher energies. The correlation with the O K edge spectra and valence band XPS shows the presence and transition of protonated μ_1 -OH to unprotonated μ_3 -O species at higher calcination temperatures as well as an SOC effect at higher temperatures and the associated shift of the t_{2g} band. The deprotonation of μ_1 -OH to produce active μ_1 -O species and the associated enhanced OER activity are also evident in the prepared samples that were calcined at lower temperatures (between 300 and 400 °C).

By the model developed in this work and the fast, vacuum-free, and non-destructive characterization with SE, in situ or operando investigations could become possible in the future. The possibility to measure the change of the Ψ and Δ spectra during electrochemical testing and the relation of the dielectric function to the energy loss function in the low-loss region would lead to a better understanding of the structure–activity relationship during electrolysis. Furthermore, SE can be applied to a wide range of materials and enable a deeper understanding of catalytic systems, batteries, and material corrosion.

ASSOCIATED CONTENT

Supporting Information

The Supporting Information is available free of charge at <https://pubs.acs.org/doi/10.1021/acscatal.0c03800>.

Experimental details including (HR)-SEM images in top-view and cross-section modes of mesoporous IrO_x films, X-ray reflectometry fitting, X-ray diffraction measurements of mesoporous iridium oxide films, electrochemical analysis of mesoporous IrO_x films, spectroscopic ellipsometry (SE) model evaluation, change of dielectric functions with calcination temperature, mean scattering time as a function of the calcination temperature of mesoporous IrO_x films, ellipsometric porosimetry (EP) measurements of mesoporous iridium oxide films, bulk electron energy loss spectra and correlation with intrinsic OER activities, resonant photoemission spectroscopy (ResPES), and X-ray photoelectron spectroscopy (XPS) (PDF)

AUTHOR INFORMATION

Corresponding Authors

Ralph Kraehnert – Faculty II Mathematics and Natural Sciences, Institute of Chemistry, Technische Universität Berlin, 10623 Berlin, Germany; Email: ralph.kraehnert@tu-berlin.de

Andreas Hertwig – Federal Institute for Materials Research and Testing (BAM), 12203 Berlin, Germany; Email: andreas.hertwig@bam.de

Authors

René Sachse – Federal Institute for Materials Research and Testing (BAM), 12203 Berlin, Germany; Faculty II Mathematics and Natural Sciences, Institute of Chemistry, Technische Universität Berlin, 10623 Berlin, Germany; orcid.org/0000-0002-3611-3352

Mika Pflüger – Physikalisch-Technische Bundesanstalt (PTB), 10587 Berlin, Germany

Juan-Jesús Velasco-Vélez – Fritz-Haber-Institut der Max-Planck-Gesellschaft, 14195 Berlin, Germany; Department of Heterogenous Reactions, Max Planck Institute for Chemical Energy Conversion, Mülheim and der Ruhr 45470, Germany; orcid.org/0000-0002-6595-0168

Mario Sahre – Federal Institute for Materials Research and Testing (BAM), 12203 Berlin, Germany

Jörg Radnik – Federal Institute for Materials Research and Testing (BAM), 12203 Berlin, Germany; orcid.org/0000-0003-0302-6815

Michael Bernicke – Faculty II Mathematics and Natural Sciences, Institute of Chemistry, Technische Universität Berlin, 10623 Berlin, Germany

Denis Bernsmeier – Faculty II Mathematics and Natural Sciences, Institute of Chemistry, Technische Universität Berlin, 10623 Berlin, Germany

Vasile-Dan Hodoroba – Federal Institute for Materials Research and Testing (BAM), 12203 Berlin, Germany

Michael Krumrey – Physikalisch-Technische Bundesanstalt (PTB), 10587 Berlin, Germany

Peter Strasser – Faculty II Mathematics and Natural Sciences, Department of Chemistry, Technical University Berlin, 10623 Berlin, Germany; orcid.org/0000-0002-3884-436X

Complete contact information is available at:

<https://pubs.acs.org/doi/10.1021/acscatal.0c03800>

Notes

The authors declare no competing financial interest.

ACKNOWLEDGMENTS

The authors would like to dedicate this work to Dr. Arnulf Röseler (1935–2020), gratefully appreciating his contributions to the development of infrared spectroscopy and ellipsometry. The project HyMET (16ENG03 Hybrid metrology for thin films in energy applications) received funding from the EMPIR program co-financed by the Participating States and from the European Union's Horizon 2020 research and innovation program. The authors thank Thorid Lange for providing XRR measurements. We also thank Ute Resch-Genger and Arne Güttler for providing UV–vis absorption spectroscopic measurements. D.B. acknowledges generous funding from VIP+ (BMBF) under contract no. FKZ 03VP05390. M.B. appreciates funding from ATOKAT (BMBF, no. FKZ 03EK3052A). The authors acknowledge BESSY II/HZB (Berlin, Germany) for allocating beam time within project no. 201-09080-CR. P. S. acknowledges partial funding by the Deutsche Forschungsgemeinschaft (DFG) through project STR 595/11-1

REFERENCES

(1) Shah, A.; Torres, P.; Tschamer, R.; Wyrsch, N.; Keppner, H. Photovoltaic Technology: The Case for Thin-Film Solar Cells. *Science* **1999**, *285*, 692–698.

(2) Tiwari, D.; Fermin, D. J.; Chaudhuri, T. K.; Ray, A. Solution Processed Bismuth Ferrite Thin Films for All-Oxide Solar Photovoltaics. *J. Phys. Chem. C* **2015**, *119*, 5872–5877.

(3) Tavakoli, M. M.; Giordano, F.; Zakeeruddin, S. M.; Grätzel, M. Mesoscopic Oxide Double Layer as Electron Specific Contact for Highly Efficient and UV Stable Perovskite Photovoltaics. *Nano Lett.* **2018**, *18*, 2428–2434.

(4) Marshall, A.; Børresen, B.; Hagen, G.; Sunde, S.; Tsyppkin, M.; Tunold, R. Iridium oxide-based nanocrystalline particles as oxygen evolution electrocatalysts. *Russ. J. Electrochem.* **2006**, *42*, 1134–1140.

(5) Nakagawa, T.; Beasley, C. A.; Murray, R. W. Efficient Electro-Oxidation of Water near Its Reversible Potential by a Mesoporous IrO_x Nanoparticle Film. *J. Phys. Chem. C* **2009**, *113*, 12958–12961.

(6) Jung, S.; McCrory, C. C. L.; Ferrer, I. M.; Peters, J. C.; Jaramillo, T. F. Benchmarking nanoparticulate metal oxide electrocatalysts for the alkaline water oxidation reaction. *J. Mater. Chem. A* **2016**, *4*, 3068–3076.

(7) Chen, S.; Zhao, Y.; Sun, B.; Ao, Z.; Xie, X.; Wei, Y.; Wang, G. Microwave-assisted Synthesis of Mesoporous Co₃O₄ Nanoflakes for Applications in Lithium Ion Batteries and Oxygen Evolution Reactions. *ACS Appl. Mater. Interfaces* **2015**, *7*, 3306–3313.

(8) Li, H.; Wei, Y.; Zhang, Y.; Yin, F.; Zhang, C.; Wang, G.; Bakenov, Z. Synthesis and electrochemical investigation of highly dispersed ZnO nanoparticles as anode material for lithium-ion batteries. *Ionics* **2016**, *22*, 1387–1393.

(9) Zhang, X.; Hou, Z.; Li, X.; Liang, J.; Zhu, Y.; Qian, Y. MoO₂ nanoparticles as high capacity intercalation anode material for long-cycle lithium ion battery. *Electrochim. Acta* **2016**, *213*, 416–422.

(10) Yang, C.; Qing, Y.; An, K.; Zhang, Z.; Wang, L.; Liu, C. Facile synthesis of the N-doped graphene/nickel oxide with enhanced electrochemical performance for rechargeable lithium-ion batteries. *Mater. Chem. Phys.* **2017**, *195*, 149–156.

(11) Reier, T.; Oezaslan, M.; Strasser, P. Electrocatalytic Oxygen Evolution Reaction (OER) on Ru, Ir, and Pt Catalysts: A Comparative Study of Nanoparticles and Bulk Materials. *ACS Catal.* **2012**, *2*, 1765–1772.

(12) Bernicke, M.; Ortel, E.; Reier, T.; Bergmann, A.; de Araujo, J. F.; Strasser, P.; Kraehnert, R. Iridium Oxide Coatings with Templated

Porosity as Highly Active Oxygen Evolution Catalysts: Structure-Activity Relationships. *ChemSusChem* **2015**, *8*, 1908–1915.

(13) Man, I. C.; Su, H.-Y.; Calle-Vallejo, F.; Hansen, H. A.; Martínez, J. I.; Inoglu, N. G.; Kitchin, J.; Jaramillo, T. F.; Nørskov, J. K.; Rossmeisl, J. Universality in Oxygen Evolution Electrocatalysis on Oxide Surfaces. *ChemCatChem* **2011**, *3*, 1159–1165.

(14) Menzel, N.; Ortel, E.; Kraehnert, R.; Strasser, P. Electrocatalysis Using Porous Nanostructured Materials. *ChemPhysChem* **2012**, *13*, 1385–1394.

(15) Menzel, N.; Ortel, E.; Mette, K.; Kraehnert, R.; Strasser, P. Dimensionally Stable Ru/Ir/TiO₂-Anodes with Tailored Mesoporosity for Efficient Electrochemical Chlorine Evolution. *ACS Catal.* **2013**, *3*, 1324–1333.

(16) Slavcheva, E.; Schnakenberg, U.; Mokwa, W. Deposition of sputtered iridium oxide—Influence of oxygen flow in the reactor on the film properties. *Appl. Surf. Sci.* **2006**, *253*, 1964–1969.

(17) Liu, D.-Q.; Yu, S.-H.; Son, S. W.; Joo, S.-K. Supercapacitive studies on IrO₂ thin film electrodes prepared by radio frequency magnetron sputtering. *Electrochem. Solid-State Lett.* **2008**, *11*, A206–A208.

(18) Petkucheva, E.; Borisov, G.; Lefterova, E.; Heiss, J.; Schnakenberg, U.; Slavcheva, E. Gold-supported magnetron sputtered Ir thin films as OER catalysts for cost-efficient water electrolysis. *Int. J. Hydrogen Energy* **2018**, *43*, 16905–16912.

(19) Casella, I. G.; Contursi, M.; Toniolo, R. Anodic electro-deposition of iridium oxide particles on glassy carbon surfaces and their electrochemical/SEM/XPS characterization. *J. Electroanal. Chem.* **2015**, *736*, 147–152.

(20) Deku, F.; Joshi-Imre, A.; Mertiri, A.; Gardner, T. J.; Cogan, S. F. Electrodeposited Iridium Oxide on Carbon Fiber Ultramicroelectrodes for Neural Recording and Stimulation. *J. Electrochem. Soc.* **2018**, *165*, D375–D380.

(21) Patil, P. S.; Chigare, P. S.; Sadale, S. B.; Seth, T.; Amalnerkar, D. P.; Kwar, R. K. Thickness-dependent properties of sprayed iridium oxide thin films. *Mater. Chem. Phys.* **2003**, *80*, 667–675.

(22) Jiang, F.; Zheng, T.; Yang, Y. Preparation and electrochromic properties of tungsten oxide and iridium oxide porous films. *J. Non-Cryst. Solids* **2008**, *354*, 1290–1293.

(23) Yoshinaga, N.; Sugimoto, W.; Takasu, Y. Oxygen reduction behavior of rutile-type iridium oxide in sulfuric acid solution. *Electrochim. Acta* **2008**, *54*, 566–573.

(24) Smith, R. D. L.; Spornova, B.; Fagan, R. D.; Trudel, S.; Berlinguette, C. P. Facile Photochemical Preparation of Amorphous Iridium Oxide Films for Water Oxidation Catalysis. *Chem. Mater.* **2014**, *26*, 1654–1659.

(25) Carmo, M.; Fritz, D. L.; Mergel, J.; Stolten, D. A comprehensive review on PEM water electrolysis. *Int. J. Hydrogen Energy* **2013**, *38*, 4901–4934.

(26) Cherevko, S.; Reier, T.; Zeradjanin, A. R.; Pawolek, Z.; Strasser, P.; Mayrhofer, K. J. J. Stability of nanostructured iridium oxide electrocatalysts during oxygen evolution reaction in acidic environment. *Electrochem. Commun.* **2014**, *48*, 81–85.

(27) Goel, A. K.; Skorinko, G.; Pollak, F. H. Optical properties of single-crystal rutile RuO₂ and IrO₂ in the range 0.5 to 9.5 eV. *Phys. Rev. B* **1981**, *24*, 7342–7350.

(28) Kwar, R. K.; Chigare, P. S.; Patil, P. S. Substrate temperature dependent structural, optical and electrical properties of spray deposited iridium oxide thin films. *Appl. Surf. Sci.* **2003**, *206*, 90–101.

(29) Hackwood, S.; Dayem, A. H.; Beni, G. Amorphous-nonmetal—to-crystalline-metal transition in electrochromic iridium oxide films. *Phys. Rev. B* **1982**, *26*, 471–478.

(30) Schulz, K.; Schmack, R.; Klemm, H. W.; Kabelitz, A.; Schmidt, T.; Emmerling, F.; Kraehnert, R. Mechanism and Kinetics of Hematite Crystallization in Air: Linking Bulk and Surface Models via Mesoporous Films with Defined Nanostructure. *Chem. Mater.* **2017**, *29*, 1724–1734.

(31) Krafft, K.; Kabelitz, A.; Siemensmeyer, K.; Schmack, R.; Bernsmeier, D.; Emmerling, F.; Kraehnert, R. Nanocasting of

Superparamagnetic Iron Oxide Films with Ordered Mesoporosity. *Adv. Mater. Interfaces* **2018**, *5*, 1700960.

(32) Bernsmeier, D.; Bernicke, M.; Schmack, R.; Sachse, R.; Paul, B.; Bergmann, A.; Strasser, P.; Ortel, E.; Kraehnert, R. Oxygen Evolution Catalysts Based on Ir–Ti Mixed Oxides with Templated Mesopore Structure: Impact of Ir on Activity and Conductivity. *ChemSusChem* **2018**, *11*, 2367–2374.

(33) Bernicke, M.; Bernsmeier, D.; Paul, B.; Schmack, R.; Bergmann, A.; Strasser, P.; Ortel, E.; Kraehnert, R. Tailored mesoporous Ir/TiO_x: Identification of structure-activity relationships for an efficient oxygen evolution reaction. *J. Catal.* **2019**, *376*, 209–218.

(34) Boissiere, C.; Grosso, D.; Lepoutre, S.; Nicole, L.; Bruneau, A. B.; Sanchez, C. Porosity and Mechanical Properties of Mesoporous Thin Films Assessed by Environmental Ellipsometric Porosimetry. *Langmuir* **2005**, *21*, 12362–12371.

(35) Gu, D.; Schüth, F. Synthesis of non-siliceous mesoporous oxides. *Chem. Soc. Rev.* **2014**, *43*, 313–344.

(36) Krins, N.; Bass, J. D.; Julián-López, B.; Evrar, P.; Boissière, C.; Nicole, L.; Sanchez, C.; Amenitsch, H.; Grosso, D. Mesoporous SiO₂ thin films containing photoluminescent ZnO nanoparticles and simultaneous SAXS/WAXS/ellipsometry experiments. *J. Mater. Chem.* **2011**, *21*, 1139–1146.

(37) Loizillon, J.; Putero, M.; Grosso, D. Tuning Mesoporous Silica Film Accessibility Through Controlled Dissolution in NH₄F: Investigation of Structural Change by Ellipsometry Porosimetry and X-ray Reflectivity. *J. Phys. Chem. C* **2019**, *123*, 30398–30406.

(38) Bindini, E.; Naudin, G.; Faustini, M.; Grosso, D.; Boissière, C. Critical Role of the Atmosphere in Dip-Coating Process. *J. Phys. Chem. C* **2017**, *121*, 14572–14580.

(39) Baklanov, M. R.; Mogilnikov, K. P.; Polovinkin, V. G.; Dultsev, F. N. Determination of pore size distribution in thin films by ellipsometric porosimetry. *J. Vac. Sci. Technol., B* **2000**, *18*, 1385–1391.

(40) Fujiwara, H. *Spectroscopic ellipsometry: principles and applications*; John Wiley & Sons: 2007, p 1–369.

(41) Tauc, J.; Menth, A. States in the gap. *J. Non-Cryst. Solids* **1972**, *8–10*, 569–585.

(42) Wooten, F. Chapter 3 - ABSORPTION AND DISPERSION. In *Optical Properties of Solids*; Wooten, F., Ed. Academic Press: 1972, pp. 42–84.

(43) Wooten, F. Chapter 4 - FREE-ELECTRON METALS. In *Optical Properties of Solids*; Wooten, F., Ed. Academic Press: 1972, pp. 85–107.

(44) Wooten, F. Chapter 5 - INTERBAND TRANSITIONS. In *Optical Properties of Solids*; Wooten, F., Ed. Academic Press: 1972, pp. 108–172.

(45) Bashara, N.; Azzam, R. *Ellipsometry and polarized light*; North-Holland Pub. Co.: 1977.

(46) Rosu, D.-M.; Ortel, E.; Hodoroaba, V.-D.; Kraehnert, R.; Hertwig, A. Ellipsometric porosimetry on pore-controlled TiO₂ layers. *Appl. Surf. Sci.* **2017**, *421*, 487–493.

(47) Ortel, E.; Hertwig, A.; Berger, D.; Esposito, P.; Rossi, A. M.; Kraehnert, R.; Hodoroaba, V.-D. New Approach on Quantification of Porosity of Thin Films via Electron-Excited X-ray Spectra. *Anal. Chem.* **2016**, *88*, 7083–7090.

(48) Martínez-Ferrero, E.; Sakatani, Y.; Boissière, C.; Grosso, D.; Fuertes, A.; Fraxedas, J.; Sanchez, C. Nanostructured Titanium Oxynitride Porous Thin Films as Efficient Visible-Active Photocatalysts. *Adv. Funct. Mater.* **2007**, *17*, 3348–3354.

(49) Ortel, E.; Reier, T.; Strasser, P.; Kraehnert, R. Mesoporous IrO₂ Films Templated by PEO-PB-PEO Block-Copolymers: Self-Assembly, Crystallization Behavior, and Electrocatalytic Performance. *Chem. Mater.* **2011**, *23*, 3201–3209.

(50) Ortel, E.; Fischer, A.; Chuenchom, L.; Polte, J.; Emmerling, F.; Smarsly, B.; Kraehnert, R. New Triblock Copolymer Templates, PEO-PB-PEO, for the Synthesis of Titania Films with Controlled Mesopore Size, Wall Thickness, and Bimodal Porosity. *Small* **2012**, *8*, 298–309.

(51) Pouchou, J.-L. X-Ray Microanalysis of Thin Surface Films and Coatings. *Microchim. Acta* **2002**, *138*, 133–152.

(52) Beckhoff, B.; Gottwald, A.; Klein, R.; Krumrey, M.; Müller, R.; Richter, M.; Scholze, F.; Thornagel, R.; Ulm, G. A quarter-century of metrology using synchrotron radiation by PTB in Berlin. *physica status solidi (b)* **2009**, *246*, 1415–1434.

(53) Krumrey, M.; Ulm, G. High-accuracy detector calibration at the PTB four-crystal monochromator beamline. *Nucl. Instrum. Methods Phys. Res., Sect. A* **2001**, *467–468*, 1175–1178.

(54) Fuchs, D.; Krumrey, M.; Müller, P.; Scholze, F.; Ulm, G. High precision soft x-ray reflectometer. *Rev. Sci. Instrum.* **1995**, *66*, 2248–2250.

(55) Ardizzone, S.; Carugati, A.; Trasatti, S. Properties of thermally prepared iridium dioxide electrodes. *J. Electroanal. Chem. Interfacial Electrochem.* **1981**, *126*, 287–292.

(56) Fierro, S.; Ouattara, L.; Calderon, E. H.; Comninellis, C. Influence of temperature on the charging/discharging process of IrO₂ coating deposited on p-Si substrate. *Electrochem. Commun.* **2008**, *10*, 955–959.

(57) Choi, W. S.; Seo, S. S. A.; Kim, K. W.; Noh, T. W.; Kim, M. Y.; Shin, S. Dielectric constants of Ir, Ru, Pt, and IrO₂: Contributions from bound charges. *Phys. Rev. B* **2006**, *74*, 205117.

(58) Brewer, S. H.; Wicaksana, D.; Maria, J.-P.; Kingon, A. I.; Franzen, S. Investigation of the electrical and optical properties of iridium oxide by reflectance FTIR spectroscopy and density functional theory calculations. *Chemical Physics* **2005**, *313*, 25–31.

(59) Tauc, J.; Grigorovici, R.; Vancu, A. Optical Properties and Electronic Structure of Amorphous Germanium. *physica status solidi (b)* **1966**, *15*, 627–637.

(60) Tauc, J. Optical Properties and Electronic Structure of Amorphous Semiconductors. In *Optical Properties of Solids*; Nudelman, S.; Mitra, S. S., Eds. Springer US: Boston, MA, 1969; pp 123–136.

(61) Wood, D. L.; Tauc, J. Weak Absorption Tails in Amorphous Semiconductors. *Phys. Rev. B* **1972**, *5*, 3144–3151.

(62) Silva, T. M.; Simões, A. M. P.; Ferreira, M. G. S.; Walls, M.; Da Cunha Belo, M. Electronic structure of iridium oxide films formed in neutral phosphate buffer solution. *J. Electroanal. Chem.* **1998**, *441*, 5–12.

(63) Zallen, R. *The physics of amorphous solids*; John Wiley & Sons: 2008, p 1–304.

(64) Brockt, G.; Lakner, H. Nanoscale EELS analysis of dielectric function and bandgap properties in GaN and related materials. *Micron* **2000**, *31*, 435–440.

(65) Prytz, Ø.; Løvrik, O. M.; Taftø, J. Comparison of theoretical and experimental dielectric functions: Electron energy-loss spectroscopy and density-functional calculations on skutterudites. *Phys. Rev. B* **2006**, *74*, 245109.

(66) Espinosa-Magaña, F.; Rosas, A.; Esparza-Ponce, H. E.; Ochoa-Lara, M. T.; Aguilar-Elguezabal, A. In situ study of the metal–insulator transition in VO₂ by EELS and ab initio calculations. *Micron* **2009**, *40*, 787–792.

(67) Egerton, R. F. *Electron energy-loss spectroscopy in the electron microscope*; Springer Science & Business Media: 2011, p 1–491.

(68) Gong, J.; Dai, R.; Wang, Z.; Zhang, Z. Thickness Dispersion of Surface Plasmon of Ag Nano-thin Films: Determination by Ellipsometry Iterated with Transmittance Method. *Sci. Rep.* **2015**, *5*, 9279.

(69) van Benthem, K.; Elsässer, C.; French, R. H. Bulk electronic structure of SrTiO₃: Experiment and theory. *J. Appl. Phys.* **2001**, *90*, 6156–6164.

(70) Zhang, Z. H.; Qi, X. Y.; Jian, J. K.; Duan, X. F. Investigation on optical properties of ZnO nanowires by electron energy-loss spectroscopy. *Micron* **2006**, *37*, 229–233.

(71) Egerton, R. F. Electron energy-loss spectroscopy in the TEM. *Rep. Prog. Phys.* **2008**, *72*, No. 016502.

(72) Erni, R.; Browning, N. D. The impact of surface and retardation losses on valence electron energy-loss spectroscopy. *Ultramicroscopy* **2008**, *108*, 84–99.

(73) Tahir, D.; Tougaard, S. Electronic and optical properties of Cu, CuO and Cu₂O studied by electron spectroscopy. *J. Phys.: Condens. Matter* **2012**, *24*, 175002.

(74) Mattheiss, L. F. Electronic structure of RuO₂, OsO₂, and IrO₂. *Phys. Rev. B* **1976**, *13*, 2433–2450.

(75) Frevel, L. J.; Mom, R.; Velasco-Vélez, J.-J.; Plodinec, M.; Knop-Gericke, A.; Schlögl, R.; Jones, T. E. In Situ X-ray Spectroscopy of the Electrochemical Development of Iridium Nanoparticles in Confined Electrolyte. *J. Phys. Chem. C* **2019**, *123*, 9146–9152.

(76) Wertheim, G. K.; Guggenheim, H. J. Conduction-electron screening in metallic oxides: IrO₂. *Phys. Rev. B* **1980**, *22*, 4680–4683.

(77) Li, T.; Kasian, O.; Cherevko, S.; Zhang, S.; Geiger, S.; Scheu, C.; Felfer, P.; Raabe, D.; Gault, B.; Mayrhofer, K. J. J. Atomic-scale insights into surface species of electrocatalysts in three dimensions. *Nat. Catal.* **2018**, *1*, 300–305.

(78) Kim, B. J.; Jin, H.; Moon, S. J.; Kim, J. Y.; Park, B. G.; Leem, C. S.; Yu, J.; Noh, T. W.; Kim, C.; Oh, S. J.; Park, J. H.; Durairaj, V.; Cao, G.; Rotenberg, E. Novel $J_{\text{eff}} = 1/2$ Mott State Induced by Relativistic Spin-Orbit Coupling in Sr₂ IrO₄. *Phys. Rev. Lett.* **2008**, *101*, No. 076402.

(79) Subedi, A. First-principles study of the electronic structure and magnetism of CaIrO₃. *Phys. Rev. B* **2012**, *85*, No. 020408.

(80) Sun, W.; Liu, J.-Y.; Gong, X.-Q.; Zaman, W.-Q.; Cao, L.-M.; Yang, J. OER activity manipulated by IrO₆ coordination geometry: an insight from pyrochlore iridates. *Sci. Rep.* **2016**, *6*, 38429.

(81) Nong, H. N.; Reier, T.; Oh, H.-S.; Gliech, M.; Paciok, P.; Vu, T. H. T.; Teschner, D.; Heggen, M.; Petkov, V.; Schlögl, R.; Jones, T.; Strasser, P. A unique oxygen ligand environment facilitates water oxidation in hole-doped IrNiOx core-shell electrocatalysts. *Nat. Catal.* **2018**, *1*, 841–851.

(82) Reier, T.; Nong, H. N.; Teschner, D.; Schlögl, R.; Strasser, P. Electrocatalytic Oxygen Evolution Reaction in Acidic Environments – Reaction Mechanisms and Catalysts. *Adv. Energy Mater.* **2017**, *7*, 1601275.

(83) Betley, T. A.; Wu, Q.; Van Voorhis, T.; Nocera, D. G. Electronic Design Criteria for O–O Bond Formation via Metal–Oxo Complexes. *Inorg. Chem.* **2008**, *47*, 1849–1861.

(84) Mavros, M. G.; Tsuchimochi, T.; Kowalczyk, T.; McIsaac, A.; Wang, L.-P.; Voorhis, T. V. What Can Density Functional Theory Tell Us about Artificial Catalytic Water Splitting? *Inorg. Chem.* **2014**, *53*, 6386–6397.